Rare Met.
https://doi.org/10.1007/s12598-024-02917-0

RARE METALS

ORIGINAL ARTICLE

Cu-doped Pd_7Te_3 nanowires for methanol oxidation under alkaline condition

Meng-Qian Li, Ze-Qun Han, Jun-Cheng Zhu, Dong-Po He, Qing Hu, Wen-Ya Fan, Qin-Yuan Hu, Xing-Chen Jiao, Qing-Xia Chen*

Received: 6 January 2024 / Revised: 21 February 2024 / Accepted: 27 March 2024
© Youke Publishing Co., Ltd. 2024

Abstract Highly active and robust electrocatalysts for methanol oxidation reaction (MOR) are of great significance to the commercial availability of alkaline direct methanol fuel cells (ADMFC). Pd-based nanostructures have received considerable attention in ADMFCs among non-platinum catalysts due to their high activity and tolerance against CO poisoning, which is strongly determined by their composition and structure. Herein, a one-spot hydrothermal method to synthesize Cu-doped Pd_7Te_3 ultrathin nanowires was proposed. The density functional theory calculations show that the Cu doping simultaneously facilitates the desorption of CO^* and adsorption of OH, which refreshes the active sites quickly and thus enhances the electroactivity for MOR. Benefiting from their ultrathin architecture and the modified bonding and anti-bonding d states of Pd, Cu-doped Pd_7Te_3 nanowires show about twofold and threefold mass activity promotion and enhanced durability for MOR when compared to the pure Pd_7Te_3 nanowires and commercial Pd/C catalysts. This work not only provides a simple one-step synthesis strategy for Pd-based nanowire catalysts, but also helps to inspire the catalyst design in ADMFC.

Keywords Cu doping; Pd_7Te_3 NWs; Methanol oxidation reaction; CO desorption; Electronic structure

1 Introduction

Alkaline direct methanol fuel cells (ADMFC) have attracted a great deal of attention due to their interest as promising alternative power sources with the growing of global energy crisis [1, 2]. The energy source methanol, known as the liquid sunlight with a high energy density, can be conveniently stored and transported [3, 4]. Additionally, the basic electrolyte membrane implies the faster kinetics for both anodic methanol and cathodic oxygen oxidation, as well as the suppressed methanol penetration. Unfortunately, the commercial availability is hindered by the low electrocatalytic activity, serious poisoning issues and high cost of mostly used Pt-based materials [5, 6]. Therefore, the development of highly efficient and durable electrocatalysts [7, 8], especially Pt-free electrocatalysts but with Pt-like performance plays a crucial role in the application of ADMFC [9, 10]. Recently, Pd nanostructures have become a promising anode electrocatalyst candidate for methanol oxidation because of their outstanding performances induced by the similar electronic structure to Pt, in which the d band is more than half filled [11–14]. Moreover, the 50-times abundance of Pd higher than Pt on the earth is also a great advantage for actual commercialization [15]. Indeed, monometallic Pd tends to

---

Meng-Qian Li, Ze-Qun Han and Jun-Cheng Zhu have contributed equally to this work.

Supplementary Information The online version contains supplementary material available at https://doi.org/10.1007/s12598-024-02917-0.

M.-Q. Li, Z.-Q. Han, D.-P. He, Q. Hu, W.-Y. Fan, Q.-Y. Hu, X.-C. Jiao, Q.-X. Chen*
Key Laboratory of Synthetic and Biological Colloids, Ministry of Education, School of Chemical and Material Engineering, Jiangnan University, Wuxi 214122, China
e-mail: qxchen@jiangnan.edu.cn

J.-C. Zhu
Hefei National Research Center for Physical Sciences at Microscale, National Synchrotron Radiation Laboratory, University of Science and Technology of China, Hefei 230026, China

Published online: 31 July 2024

preferentially adsorb CO, leading to the poisoning of Pd active sites and degradation of activity and stability. Therefore, it is still very challenging to further enhance the activity and circumvent the adsorption of CO intermediates on monometallic Pd electrocatalysts.

To overcome the limitations, many efforts have been dedicated to optimize Pd electrocatalysts by modulating the population and shifting of d band, and providing OH^* to boost the oxidation of adsorbed CO^* into CO_2, such as developing bimetallic and alloyed Pd-based electrocatalysts [16, 17]. It is supposed that the incorporation of dopant atoms not only provides more active sites, but also alters the inherent electronic structure of Pd-based electrocatalyst with more facilitated electron transfer during methanol oxidation reaction (MOR) [18, 19]. The introduction of dopant atoms, especially the late transition metals, will causes a shifting of d band center to remain the fixed d occupancy. This would lead to a corresponding movement of anti-bonding d state and the change of adsorption interaction, which consequently steers a superior electrocatalytic activity [20]. More importantly, the introduction of nonprecious transition metals can steer the formation of OH^* species, which can further oxidize the CO^* adsorbed on adjacent Pd sites. For example, Fe-doped Pd nanocages displayed an excellent MOR activity of $1075.5\ mA \cdot mg^{-1}$ compared with Pd nanoparticles, resulting from the downshift of d band center of Pd induced by Fe addition [21]. Ni-doped Pd nanoparticles exhibited an ethanol oxidation activity of $2368.22\ mA \cdot mg^{-1}$ in alkaline electrolyte, higher than other reported Pd-based electrocatalysts [22]. This is due to that $Ni(OH)_2$ formed during the reaction absorbs OH, leading to the local enrichment of OH^* and further refreshment of Pd active sites. The incorporation of Co into Pd nanospheres also enables a higher MOR property of $1488\ mA \cdot mg^{-1}$ due to the synergistic effects between Pd and Co atoms, which regulates the electronic structure and thus promotes the electron and mass transfer [23]. Inspired by this, the desorption of CO^*, as well as the favorable adsorption of OH, can be promoted by the doping of oxyphilic Cu with a half-empty 4 s orbital, which can reduce the d band center of Pd and thus enhance the MOR activity and stability [24].

In this work, binary phases of palladium tellurides, Pd_7Te_3 nanowires (NWs), were selected as prototype Pd-based catalysts due to the rich surface sites resulted from their ultrathin diameter and the fast electron conductivity and self-supporting ability imparted by one-dimensional (1D) structure [25]. More importantly, the abundant Te defects in Pd_7Te_3 NWs, which can effectively stabilize the dopant atoms [26, 27]. The oxyphilic Cu was incorporated into Pd_7Te_3 NWs to regulate the electronic structure of Pd and the binding of intermediate CO^* and OH. An excellent MOR activity of $1680\ mA \cdot mg^{-1}$ under alkaline condition was demonstrated in comparation with pure Pd_7Te_3 NWs and commercial Pd/C catalysts. In the meanwhile, Cu-doped Pd_7Te_3 NWs displayed an outstanding stability on account of the constantly refreshed Pd active sites derived from the synergistic effect between CO^* desorption and OH adsorption, as well as the prevented aggregation and ripening thanks to the 1D self-supported structure. This work offers an effective doping strategy to manipulate the CO and OH binding on Pd-based catalysts during the oxidation of small alcohols in alkaline medium.

2 Results and discussion

2.1 Doping Cu into Pd_7Te_3 NWs

Ultrathin Cu/Pd_7Te_3 NW electrocatalysts were fabricated via a one-step hydrothermal approach (Supporting Information for details). The typical synthesis procedure is illustrated in Fig. 1a. Highly uniform Te NWs [28] were employed as templates for Pd_7Te_3 NWs combination with the presence of Cu precursor. Cu atoms enter into the lattice of Pd_7Te_3 with a weight doping ratio of 0.2 wt%. It is worth mentioning that the post-washing process, including the alkaline treatment, pickling and water scrubbing in turn, plays an important role in the sample purification [27]. For comparison, Pd_7Te_3 NWs without Cu doping were also prepared in a similar pathway, except without the Cu source addition. The morphological and structural characterizations and elemental distribution of the obtained electrocatalysts are summarized in Fig. 1b–i. TEM image (Fig. 1b) demonstrates that the as-synthesized products are nanowires with a diameter of about 9.5 nm (Fig. S1), inheriting the morphology of Te NW templates. High-resolution transmission electron microscopy (HRTEM) image of Cu/Pd_7Te_3 NWs (Fig. 1c) reveals the clear lattice fringe of 0.22 nm corresponding to the (004) planes in Pd_7Te_3. Moreover, no deposited nanoparticles (NPs) or clusters on the surface of Cu/Pd_7Te_3 NWs can be noticed from HRTEM images, suggesting that Cu atoms were uniformly distributed rather than being concentrated in separate NPs or clusters on the surface of NWs. In addition, X-ray diffractometer (XRD) measurement was employed to determine the crystalline structures of both Cu/Pd_7Te_3 and pure Pd_7Te_3 NWs. As displayed in Fig. 1d, XRD patterns of pure and Cu-doped Pd_7Te_3 NWs show little differences. Specifically, the diffraction peak located at 40.1° is assigned to the (004) planes of cubic Pd_7Te_3 (JCPDS No. 43-1294), which corroborates well with those reported previously [29, 30]. No peaks can be pointed to Cu or CuO. This confirms the successful incorporation of Cu atoms into the Pd_7Te_3 lattice, which remains intact. Noteworthily, it is also difficult to identify isolated and

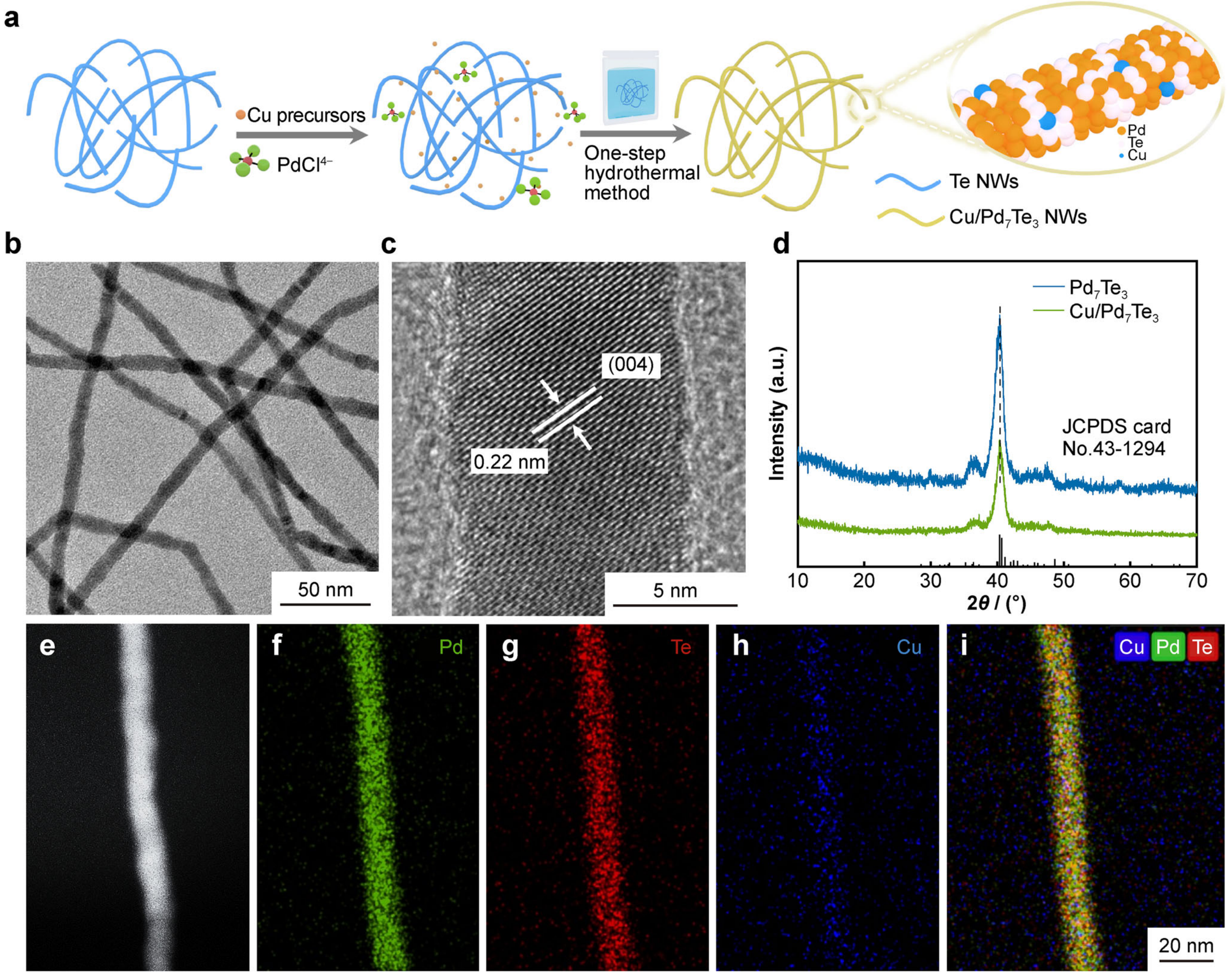

Fig. 1 Schematic illustration and characterization of Cu/Pd_7Te_3 NWs: **a** schematic illustration for one-step hydrothermal preparation of Cu/Pd_7Te_3 NWs; **b** TEM image, **c** HRTEM image and **d** XRD patterns of Cu/Pd_7Te_3 NWs and Pd_7Te_3 NWs; **e** HADDF-STEM image and **f–i** EDS maps of Cu/Pd_7Te_3 NWs

attached NPs nearby the NWs from scanning transmission electron microscopy (STEM) image (Fig. 1e), further verifying the effective atomic doping of Cu. Moreover, energy dispersive spectroscopy (EDS) maps of Cu/Pd_7Te_3 NWs (Fig. 1f–i) indicate the uniform distribution of Pd, Te and Cu along the NWs. Figure S2 displays high-angle annular dark-field(HAADF) image and line-scan profile across a Cu/Pd_7Te_3 NWs, further proving the formation of a uniform component distribution and Cu doping. The morphological and structural characterizations of pure Pd_7Te_3 NWs were shown in Figs. S3, S4. A similar lattice fringe of 0.22 nm can also be observed in HRTEM image of Pd_7Te_3 NWs in Fig. S3d. The uniform Pd and Te distribution in Pd_7Te_3 NWs can be confirmed by the element mapping and line-scan profile in Fig. S4.

To further prove the successful doping of Cu, X-ray photoelectron spectroscopy (XPS) spectra of Cu-doped and undoped Pd_7Te_3 NWs were both collected. According to the comparison of survey spectra in Fig. S5, the peak centered at 934 eV in Cu/Pd_7Te_3 NWs is indexed to Cu, while no noticeable signals of Cu are probed in pure Pd_7Te_3 NWs. Furthermore, high-resolution XPS characterization of Cu/Pd_7Te_3 NWs in Fig. 2a obviously exhibits the peak of Cu 2p orbital, which is absent in that of pure Pd_7Te_3 NWs, manifesting the existence of Cu in doped Pd_7Te_3 NWs. The fitted analysis of Cu 2p region in Fig. 2b exhibits that the peaks of Cu $2p_{3/2}$ and Cu $2p_{1/2}$ are centered at 934.2 and 953.8 eV, respectively. In addition to these two sets of peaks, there is another set of satellite peaks positioned at 942.8 and 961.9 eV, which is consistent with the previous report [31]. This is further evidenced by the Cu L-edge X-ray absorption near-edge spectroscopy (XANES) spectra in Fig. 2c, which shows the Cu absorption energy in Cu/Pd_7Te_3 NWs [32] while no noticeable

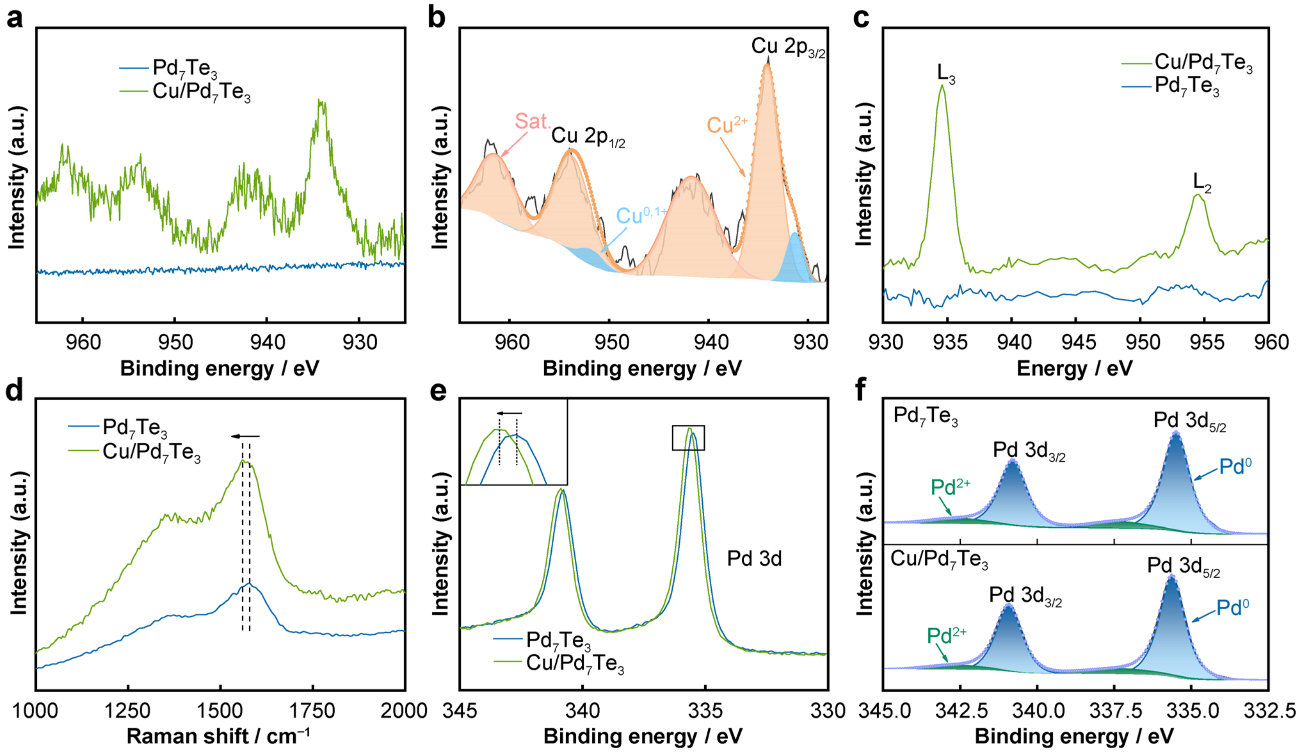

Fig. 2 Structural characterization of Cu/Pd$_7$Te$_3$ NWs: **a** high-resolution XPS spectra of Cu 2p orbital of Pd$_7$Te$_3$ and Cu/Pd$_7$Te$_3$ NWs; **b** deconvoluted Cu 2p fine XPS spectra of Cu/Pd$_7$Te$_3$ NWs; **c** Cu L-edge XANES spectra of Cu/Pd$_7$Te$_3$ and pure Pd$_7$Te$_3$ NWs; **d** Raman spectra of Pd$_7$Te$_3$ and Cu/Pd$_7$Te$_3$ NWs; **e** high-resolution XPS spectra of Pd 3d orbital of Pd$_7$Te$_3$ and Cu/Pd$_7$Te$_3$ NWs; **f** deconvoluted Pd 3d fine XPS spectra of Pd$_7$Te$_3$ and Cu/Pd$_7$Te$_3$ NWs

single peaks from Cu are observed in the pure Pd$_7$Te$_3$ NWs. Raman spectra in Fig. 2d show a significant downshift from 1578 cm^{-1} of pure Pd$_7$Te$_3$ to1558 cm^{-1} of doped NWs, which implies that the incorporation of Cu causes the lattice deformation of Pd$_7$Te$_3$. In ordered to quantitatively determine the actual Cu loading ratio, the inductively coupled plasma optical emission spectrometry (ICP-OES) measurement was conducted, which directly suggests that the weight ratio of Cu in Cu/Pd$_7$Te$_3$ NWs is 0.2wt%.

To clarify the electron structures of Pd in both Cu-doped and pure Pd$_7$Te$_3$ NWs, XPS spectra of Pd 3d core levels were analyzed. As demonstrated in Fig. 2e, the binding energy of Pd 3d$_{2/3}$ in Cu/Pd$_7$Te$_3$ NWs shows an upshifting compared to Pd$_7$Te$_3$ NWs. The positive shift is the consequence of electron transfer from the neighboring Cu atoms to Pd atoms. With this modification of electronic structure, more desired OH* enrichment on Pd active sites is enabled. This can be more clearly observed in Fig. 2f. As shown in Fig. 2f, the peak-fit analysis of Pd 3d XPS spectra disclose the two doublets in both undoped and doped Pd$_7$Te$_3$ NWs (Pd 3d$_{5/2}$ peaks located at 335.5 and 335.7 eV, the corresponding Pd 3d$_{3/2}$ peaks at 340.7 and 340.9 eV respectively), which can be assigned to Pd and PdO [33–35]. The larger binding energy of Pd 3d for Cu/Pd$_7$Te$_3$ NWs than that of pure Pd$_7$Te$_3$ NWs implies a strong electronic interaction in Cu/Pd$_7$Te$_3$ NWs, which would greatly regulate the surface electronic structure of catalysts, thereby promoting their electrocatalytic performances. The Te 3d orbital spectra of Cu/Pd$_7$Te$_3$ and Pd$_7$Te$_3$ NWs were shown in Fig. S6, in which a small amount of Te^{4+} appear due to the partial oxidation of Te in air.

2.2 Electrocatalytic performances of Cu/Pd$_7$Te$_3$ NWs for MOR

The MOR under alkaline condition was utilized as a model reaction to investigate the structure–activity relationship of the obtained Cu/Pd$_7$Te$_3$ NWs, and their MOR performances were compared with pure Pd$_7$Te$_3$ NWs and commercial Pd/C catalysts. Figure 3a displays cyclic voltammetry (CV) profiles of these three catalysts in N$_2$-bubbled 1.0 mol·L^{-1} KOH solution with a sweep rate of 50 mV·s^{-1} at room temperature, showing the characteristic features of Pd. Specifically, the peaks at − 0.18 V (vs. Ag/AgCl) scan forward and − 0.49 V (vs. Ag/AgCl) scan backward are ascribed to the oxidation of Pd and reduction of Pd oxides, respectively. Cu/Pd$_7$Te$_3$ NWs have larger reduction peak of Pd oxides than pure Pd$_7$Te$_3$ NWs and Pd/C, reflecting a larger electrochemically active surface area

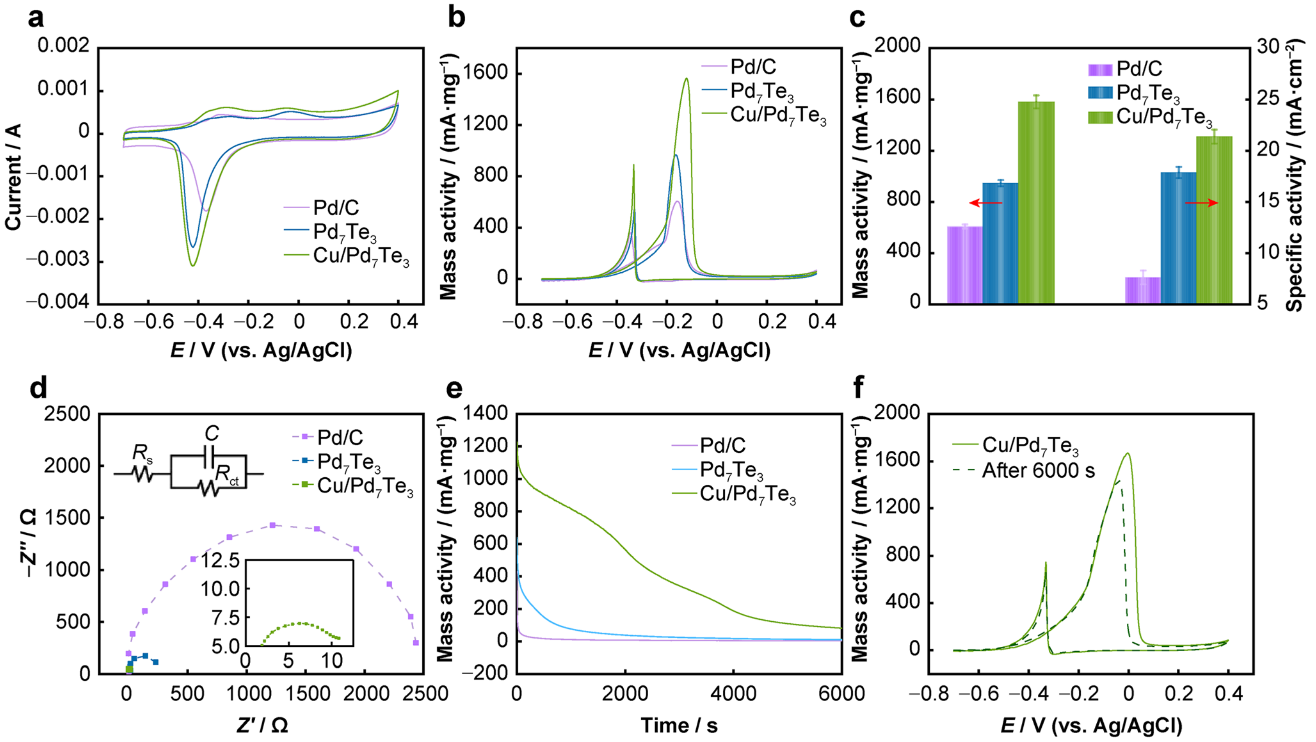

Fig. 3 Electrocatalytic MOR performances of Pd_7Te_3 NWs, Cu/Pd_7Te_3 NWs and commercial Pd/C catalysts: **a** CV curves in 1.0 $mol·L^{-1}$ KOH solution at a scan rate of 50 $mV·s^{-1}$; **b** MOR profiles in 1.0 $mol·L^{-1}$ KOH + 1.0 $mol·L^{-1}$ CH_3OH solution at a scan rate of 50 $mV·s^{-1}$; **c** histogram of mass activities and specific activities of different catalysts; **d** Nyquist plots of three catalysts in 1.0 $mol·L^{-1}$ KOH + 1.0 $mol·L^{-1}$ CH_3OH solution and (inset) equivalent circuit; **e** chronoamperometry curves for MOR at − 0.18 V of the three catalysts in 1.0 $mol·L^{-1}$ KOH + 1.0 $mol·L^{-1}$ CH_3OH solution for 6000 s; **f** MOR profiles of Cu/Pd_7Te_3 NWs before and after chronoamperometry test

(ECSA) [36, 37]. By integrating the charge of reduction peak from − 0.55 to − 0.08 V based on CV profiles after 200 cycles (Fig. S7a), ECSA of Cu/Pd_7Te_3, pure Pd_7Te_3 NWs and Pd/C are calculated as 72.8, 70.7 and 76.8 $m^2·g^{-1}$ (Fig. S7b), respectively, based on Pd content. A rougher surface can be observed in Cu/Pd_7Te_3 NWs after 200 CV cycles shown in Fig. S8. The detailed calculation of ECSA is described in the Supporting Information. The CV analysis was also employed to evaluate the MOR performances of these three catalysts. Upon adding CH_3OH into the alkaline electrolyte, two evident oxidation peaks arise scan forward and backward, which are ascribed to the characteristic peaks of MOR. The MOR profiles in Fig. 3b shows that Cu/Pd_7Te_3 NWs exhibit a mass activity of 1.68 $A·mg^{-1}$, 1.83 and 2.85-fold improvement over that of pure Pd_7Te_3 NWs (0.92 $A·mg^{-1}$) and Pd/C (0.59 $A·mg^{-1}$), respectively. The histograms of mass activities for MOR over these three catalysts are shown in Fig. 3c. The specific activity of Cu/Pd_7Te_3 NWs is also the highest among all these three Pd-based catalysts (21.49, 17.66 and 7.8 $mA·cm^{-2}$, respectively). As also observed from Fig. S7b, the peak current density ratio of the forward scan to backward scan (I_f/I_b) of Cu/Pd_7Te_3 NWs is 1.90, which is also higher than that of Pd_7Te_3 NWs (1.61) and Pd/C catalysts (1.67). This demonstrates that the Cu/Pd_7Te_3 NWs possess a better ability of resistance poisoning to CO and other carbonaceous species [38, 39], hinting a more favorable CO^* removal and surface refreshing behavior, which contributes to the MOR activity promotion of Cu/Pd_7Te_3 NWs. And this resistance to CO poisoning was further verified by the anti-CO poisoning experiments. As shown in Fig. S9, the peak position of Cu/Pd_7Te_3 NWs was at –0.31 V. This more negative peak position compared with that of undoped Pd_7Te_3 NWs (–0.24 V) and commercial Pd/C catalysts (–0.14 V) suggests that Cu/Pd_7Te_3 NWs exhibit an enhanced tolerance to CO poisoning. The performance of Cu/Pd_7Te_3 NWs in this work was compared with other previously reported Pd-based catalysts, exhibiting high activity and durability for MOR under alkaline condition (Fig. S10 and Table S1).

In order to investigate the charge transfer resistance (R_{ct}), the electrochemical impedance spectroscopy (EIS) was carried out and an equivalent circuit was fitted. The Nyquist plots of these three electrocatalyst in methanol alkaline medium, as shown in Fig. 3d, show a smaller charge transfer resistance (R_{ct}) value for Cu/Pd_7Te_3 NWs than pure Pd_7Te_3 NWs and Pd/C catalysts, indicating a better electron transport between electrodes facilitated by

Cu doping. This confirms the stable provision of a conduction pathway in ADMFC system by Cu/Pd_7Te_3 NWs. To further explore the durability of the as-obtained catalysts, the chronoamperometry test was recorded at − 0.18 V (vs. Ag/AgCl). As indicated by Fig. 3e, the current density on Cu/Pd_7Te_3 NWs is higher than that of undoped Pd_7Te_3 NWs and Pt/C during the whole measurement process. After 6000 s, Cu/Pd_7Te_3 NWs retain an activity of 86.0% of the initial values, providing a better long-term stability for MOR (Fig. 3f). The high-quality NW structure of Cu/Pd_7Te_3 NWs was remained and no extensive agglomeration or severe ripening were observed after long-term stability tests (Fig. S11a). And the lattice structure of Cu/Pd_7Te_3 NWs after chronoamperometry also remains intact (Fig. S11b). All these results show that Cu/Pd_7Te_3 NWs are highly active and durable for MOR in strong alkaline solution. The CV profile after 200 cycles and TEM image of pure Pd_7Te_3 NWs were also exhibited in Fig. S12, indicating a similar surface roughness behavior in pure Pd_7Te_3 NWs during CV cycles. Additionally, the consecutive CV tests for 500 cycles in 1.0 $mol \cdot L^{-1}$ KOH + 1.0 $mol \cdot L^{-1}$ CH_3OH solution with a scan rate of 100 $mV \cdot s^{-1}$ was also conducted to further demonstrate the stability of Cu/Pd_7Te_3 NWs. The result in Fig. S13 indicates that the mass activity of Cu/Pd_7Te_3 NWs was retained by about 70%, which shows that Cu/Pd_7Te_3 NWs have an excellent cycling stability in alkaline medium.

2.3 Insights into CO* desorption and OH adsorption

Based on the previous study, the overall reaction and electrode reactions of MOR process on Pd-based catalysts in alkaline medium are shown in the following reactions [40–42], respectively.

$$2CH_3OH + 3O_2 \rightarrow 2CO_2 \uparrow + 4H_2O \quad (\text{Overall reaction}) \tag{1}$$

$$CH_3OH + 6OH^- \rightarrow CO_2 \uparrow + 5H_2O + 6e^- \quad (\text{Anodic reaction}) \tag{2}$$

$$O_2 + 2H_2O + 4e^- \rightarrow 4OH^- \quad (\text{Cathodic reaction}) \tag{3}$$

CH_3OH is oxidized into CO_2 in anode half reaction accompanied by a six-electron transfer process. And the possible mechanism can be described as follows.

$$Pd + OH^- \rightarrow Pd(OH)_{ads} + e^- \tag{4}$$

$$Pd + (CH_3OH)_{ads} \rightarrow Pd(CH_3OH)_{ads} \tag{5}$$

$$Pd(CH_3OH)_{ads} + OH^- \rightarrow Pd_2(CH_3O)_{ads} + H_2O + e^- \tag{6}$$

$$Pd(CH_3O)_{ads} + OH^- \rightarrow Pd(CH_2O)_{ads} + H_2O + e^- \tag{7}$$

$$Pd(CH_2O)_{ads} + OH^- \rightarrow Pd(CHO)_{ads} + H_2O + e^- \tag{8}$$

$$Pd(CHO)_{ads} + OH^- \rightarrow Pd(CO)_{ads} + H_2O + e^- \tag{9}$$

$$Pd(CO)_{ads} + Pd(OH)_{ads} + OH^- \rightarrow 2Pd + CO_2 \uparrow + H_2O + e^- \tag{10}$$

OH^- and CH_3OH in the bulk electrolyte are firstly absorbed onto the Pd active sites. Then, the CH_3OH_{ads} is dehydrogenated stepwise into CO^* in the presence of OH^-. Finally, CO^* is further oxidized to CO_2 under OH^* and OH^-, leaving the catalyst surface and diffusing into the bulk electrolyte. As is well-known, CO^* and other carbonaceous reactive intermediates can strongly absorb onto and block the Pd active sites [43]. With OH^* on Pd sites, the absorbed carbonaceous intermediates can be rapidly stripped away, refreshing the active sites. And an increasing current will be steered. Therefore, CH_3OH oxidation is significantly determined by the coverage degree of both OH and CO.

To shed light on the high-MOR performance on Cu-doped Pd_7Te_3 NWs, density functional theory (DFT) calculations are performed to further explore the precise atomic configurations as well as the underlying CO and OH adsorption and removal behavior on both doped and undoped NWs. Here, we modeled a (004) facet due to its dominance in both two NWs (Fig. 4a–d). As disclosed by Fig. 4e, f, the reaction barrier of CO^* desorption over the Cu-doped Pd_7Te_3 NWs was 1.22 eV, which was lower than that of pure Pd_7Te_3 NWs (1.28 eV). This suggests an easier desorption of CO^* after the Cu doping in Pd_7Te_3 NWs. Moreover, OH absorption on doped and undoped Pd_7Te_3 NWs was also constructed (Fig. 4c, d). Interestingly, the lower reaction barrier of OH adsorption for the doped NWs (1.055 eV) than undoped NWs (1.255 eV) (Fig. 4e, g) also indicates that the introduction of Cu was in favor of the OH adsorption during MOR process. These results are attributed to the fact that Cu doping causes the electron aggregation form Cu atom to the neighboring Pd atom, as exhibited in the differential charge density maps and calculated Bader charge values in Fig. 4h and i. The charge-rich Pd atom acts as the active sites to anchor the electron-attracting OH and repel the electron-donating CO, and hence boosts the MOR performance. This can also be confirmed by the upshifting in the Pd 3d orbital XPS spectra (Fig. 2a). Therefore, the mechanism of enhanced MOR properties over Cu/Pd_7Te_3 NWs can be explained by the electronic effect of simultaneously boosted CO^* desorption and OH adsorption (Fig. 4j). The Cu atom doping regulates the electronic structure of Pd, which reduces the CO adsorption energy and favors the C-H cleavage. This means that Cu/Pd_7Te_3 NWs remove the CO^* and other carbonaceous species easier than undoped Pd_7Te_3 NWs. On the other side, Cu doping also decreases OH adsorption energy on Pd site, which facilitates the formation of Pd-OH

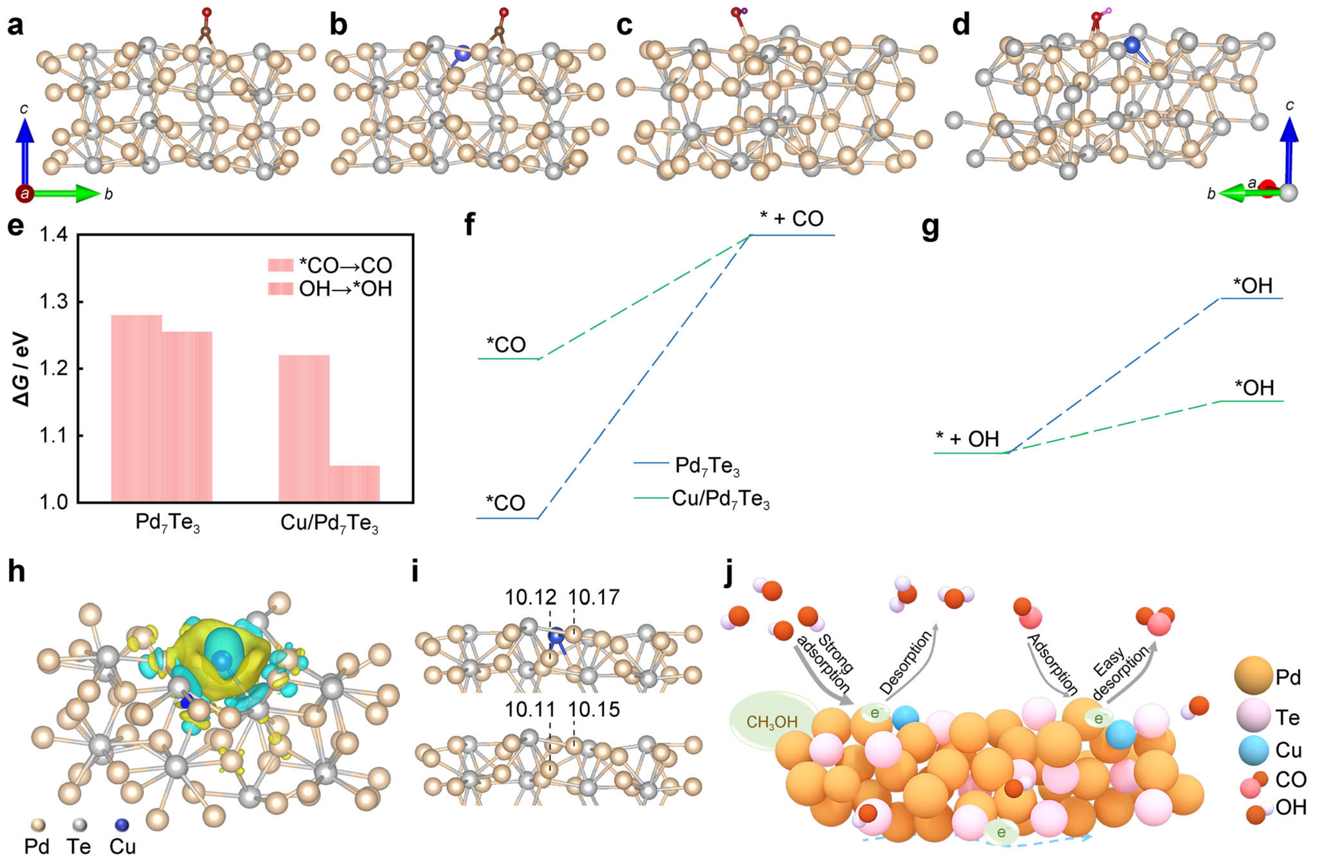

Fig. 4 Mechanism for MOR over Pd_7Te_3 and Cu/Pd_7Te_3 NW catalyst: DFT calculations of **a** CO, **c** OH adsorption on Pd_7Te_3 NWs and **b** CO, **d** OH adsorption on Cu/Pd_7Te_3 NWs; **e** Gibbs free energy of CO^* desorption and OH adsorption on Pd_7Te_3 NWs and Cu/Pd_7Te_3 NWs; free energy diagram of **f** CO^* desorption and **g** OH adsorption on Pd_7Te_3 NWs and Cu/Pd_7Te_3 NWs; **h** differential charge density distributions on Pd and Cu atoms in Cu/Pd_7Te_3 NWs; **i** calculated Bader charge values for for Pd_7Te_3 and Cu/Pd_7Te_3 NWs. **j** CH_3OH oxidation mechanism over Cu/Pd_7Te_3 NW catalyst

and thus the dehydrogenation of CH_3OH. The easier OH adsorption is also conducive to the CO oxidation and subsequent release from the surface sites. For the undoped Pd_7Te_3 NWs, CO^* desorption and OH adsorption are both relatively difficult, leading a seriously sluggish oxidation kinetic for the overall MOR process.

3 Conclusion

To summarize, we have developed a simple one-step hydrothermal method to create Cu doping on Pd_7Te_3 NWs, which simultaneously facilitates the CO^* desorption and OH adsorption, continuously refreshing the active sites for CH_3OH oxidation. In addition, the enhanced OH adsorption on the doped Pd sites delivers electrons to CO^* and other carbonaceous intermediates, which holds the key to quick oxidation and subsequently efficient removal of CO^* and other carbonaceous intermediates. Therefore, the Cu/Pd_7Te_3 NWs achieve an impressive MOR activity of 1.68 $A{\cdot}mg^{-1}$ under alkaline condition, 1.83 and 2.85 folds higher than undoped NWs and commercial Pd/C catalysts, respectively. Moreover, the Cu doping significantly improved the antitoxic ability to CO and other carbonaceous intermediates, outperforming those of undoped Pd_7Te_3 NWs and commercial Pd/C catalysts, which makes Cu/Pd_7Te_3 NWs a highly active and stable catalyst for MOR. This work powerfully demonstrates that the heteroatom doping engineering can serve as an effective strategy to regulate the electronic structure in catalyst design and tailoring at atomic precision, contributing to develop highly active and durable anode catalysts for ADMCF in alkaline medium.

Acknowledgements This work was financially supported by the National Natural Science Foundation of China (Nos. 22275178 and 22005285) and the Fundamental Research Funds for the Central Universities (Nos. JUSRP123013 and JUSRP123015). Numerical computations were performed on Hefei advanced computing center. Supercomputing USTC and National Supercomputing Center in Shenzhen are acknowledged for computational support.

Declarations

Conflict of interests The authors declare that they have no conflict of interest.

References

[1] Chen SF, Liu N, Zhong JJ, Yang RL, Yan B, Gan LY, Yu P, Gui XC, Yang HB, Yu DS, Zeng ZP, Yang GW. Engineering support and distribution of palladium and tin on MXene with the modulation d-band center for CO-resilient methanol oxidation. Angew Chem-Int Edit. 2022;61(45):e2022096. https://doi.org/10.1002/anie.202209693.

[2] Zerdoumi R, Matselko O, Rössner L, Sarkar B, Grin Y, Armbrüster M. Disentangling electronic and geometric effects in electrocatalysis through substitution in isostructural intermetallic compounds. J Am Chem Soc. 2022;144(18):8379. https://doi.org/10.1021/jacs.2c03348.

[3] Araya SS, Liso V, Cui XT, Li N, Zhu JM, Sahlin SL, Jensen SH, Nielsen MP, Kær SK. A review of the methanol economy: the fuel cell route. Energies. 2020;13(3):596. https://doi.org/10.3390/en13030596.

[4] Ranjekar AM, Yadav GD. Steam reforming of methanol for hydrogen production: a critical analysis of catalysis, processes, and scope. Ind Eng Chem Res. 2021;60(1):89. https://doi.org/10.1021/acs.iecr.0c05041.

[5] Cao SY, Ye F, Zhang NN, Guo YL, Guo Y, Wang L, Dai S, Zhan WC. Synergistic effect of bimetallic RuPt/TiO_2 catalyst in methane combustion. Rare Met. 2023;42(1):165. https://doi.org/10.1007/s12598-022-02118-7.

[6] Antolini E. Palladium in fuel cell catalysis. Energy Environ Sci. 2009;2(9):915. https://doi.org/10.1039/b820837a.

[7] Huang YF, Wu P, Tang JP, Yang J, Li J, Chen S, Zhao XL, Chen C, Zhang BW, Ma YY, Shi WH, Lin DH, Sun SG. MOF-derived Cu embedded into N-doped mesoporous carbon as a robust support of PdAu nanocatalysts for ethanol electrooxidation. Rare Met. 2023. https://doi.org/10.1007/s12598-023-02512-9.

[8] Zhang Q, Yan MM, Du WF, Yin CY, Zhang J, Yang L, Kang YQ, He HY, Huang HJ. Spatial construction of ultrasmall Pt-decorated 3D spinel oxide-modified N-doped graphene nanoarchitectures as high-efficiency methanol oxidation electrocatalysts. Rare Met. 2024;43(1):186. https://doi.org/10.1007/s12598-023-02418-6.

[9] Kang YQ, Xue Q, Zhao Y, Li XF, Jin PJ, Chen Y. Selective etching induced synthesis of hollow Rh nanospheres electrocatalyst for alcohol oxidation reactions. Small. 2018;14(29):10. https://doi.org/10.1002/smll.201801239.

[10] Guo Y, Yang XB, Liu XC, Tong XL, Yang NJ. Coupling methanol oxidation with hydrogen evolution on bifunctional Co-doped Rh electrocatalyst for efficient hydrogen generation. Adv Funct Mater. 2023;33(2):10. https://doi.org/10.1002/adfm.202209134.

[11] Xu BY, Zhang Y, Li LG, Shao Q, Huang XQ. Recent progress in low-dimensional palladium-based nanostructures for electrocatalysis and beyond. Coord Chem Rev. 2022;459:214388. https://doi.org/10.1016/j.ccr.2021.214388.

[12] Meng H, Zeng DR, Xie FY. Recent development of Pd-based electrocatalysts for proton exchange membrane fuel cells. Catalysts. 2015;5(3):1221. https://doi.org/10.3390/catal5031221.

[13] Si LX, Li H, Zhang Y, Zhang DH, An XW, Yao MM, Shao YY, Zhu JS, Hu S. Shape-dependence in seeded-growth of Pd-Cu solid solution from Pd nanostructure towards methanol oxidation electrocatalyst. Nano Res. 2023;16(7):9116. https://doi.org/10.1007/s12274-023-5741-8.

[14] Wang TJ, Li FM, Huang H, Yin SW, Chen P, Jin PJ, Chen Y. Porous Pd-PdO nanotubes for methanol electrooxidation. Adv Funct Mater. 2020;30(21):2000534. https://doi.org/10.1002/adfm.202000534.

[15] Xu H, Shang HY, Wang C, Du YK. Recent progress of ultrathin 2D Pd-based nanomaterials for fuel cell electrocatalysis. Small. 2021;17(5):2005092. https://doi.org/10.1002/smll.202005092.

[16] Gao F, Zhang YP, Song PP, Wang J, Yan B, Sun QW, Li L, Zhu X, Du YK. Shape-control of one-dimensional PtNi nanostructures as efficient electrocatalysts for alcohol electrooxidation. Nanoscale. 2019;11(11):4831. https://doi.org/10.1039/c8nr09892a.

[17] Zhang YP, Gao F, You HM, Li ZL, Zou B, Du YK. Recent advances in one-dimensional noble-metal-based catalysts with multiple structures for efficient fuel-cell electrocatalysis. Coord Chem Rev. 2022;450:19. https://doi.org/10.1016/j.ccr.2021.214244.

[18] Li HD, Han Y, Zhao H, Qi WJ, Zhang D, Yu YD, Cai WW, Li SX, Lai JP, Huang BL, Wang L. Fast site-to-site electron transfer of high-entropy alloy nanocatalyst driving redox electrocatalysis. Nat Commun. 2020;11(1):5437. https://doi.org/10.1038/s41467-020-19277-9.

[19] Wang MJ, Li LG, Wang MM, Huang XQ. Recent progress in palladium-nonmetal nanostructure development for fuel cell applications. Npg Asia Mater. 2022;14(1):78. https://doi.org/10.1038/s41427-022-00423-2.

[20] Luo MC, Guo SJ. Strain-controlled electrocatalysis on multimetallic nanomaterials. Nat Rev Mater. 2017;2(11):17059. https://doi.org/10.1038/natrevmats.2017.59.

[21] Xu H, Shang HY, Wang C, Jin LJ, Chen CY, Du YK. Nanoscale engineering of porous Fe-doped Pd nanosheet assemblies for efficient methanol and ethanol electrocatalyses. Nanoscale. 2020;12(3):2126. https://doi.org/10.1039/c9nr09755d.

[22] Zhang ZY, Xin L, Sun K, Li WZ. Pd-Ni electrocatalysts for efficient ethanol oxidation reaction in alkaline electrolyte. Int J Hydrog Energy. 2011;36(20):12686. https://doi.org/10.1016/j.ijhydene.2011.06.141.

[23] Sheng GQ, Chen JH, Ye HQ, Hu ZX, Fu XZ, Sun R, Huang WX, Wong CP. Hollow PdCo alloy nanospheres with mesoporous shells as high-performance catalysts for methanol oxidation. J Colloid Interface Sci. 2018;522:264. https://doi.org/10.1016/j.jcis.2018.03.039.

[24] Fan JC, Yu SS, Qi K, Liu C, Zhang L, Zhang HY, Cui XQ, Zheng WT. Synthesis of ultrathin wrinkle-free PdCu alloy nanosheets for modulating d-band electrons for efficient methanol oxidation. J Mater Chem A. 2018;6(18):8531. https://doi.org/10.1039/c8ta01912f.

[25] Li MG, Xia ZH, Luo MC, He L, Tao L, Yang WW, Yu YS, Guo SJ. Structural regulation of Pd-based nanoalloys for advanced electrocatalysis. Small Sci. 2021;1(11):2100061. https://doi.org/10.1002/smsc.202100061.

[26] Kim WS, Chao GY, Cabri LJ. Phase relations in the Pd-Te system. J Less-Common Met. 1990;162(1):61. https://doi.org/10.1016/0022-5088(90)90459-W.

[27] Jiao JQ, Lin R, Liu SJ, Cheong WC, Zhang C, Chen Z, Pan Y, Tang JG, Wu KL, Hung SF, Chen HM, Zheng LR, Lu Q, Yang X, Xu BJ, Xiao H, Li J, Wang DS, Peng Q, Chen C, Li YD. Copper atom-pair catalyst anchored on alloy nanowires for selective and efficient electrochemical reduction of CO_2. Nat Chem. 2019;11(3):222. https://doi.org/10.1038/s41557-018-0201-x.

[28] Qian HS, Yu SH, Gong JY, Luo LB, Fei LF. High-quality luminescent tellurium nanowires of several nanometers in diameter and high aspect ratio synthesized by a poly (vinyl pyrrolidone)-assisted hydrothermal process. Langmuir. 2006;22(8):3830. https://doi.org/10.1021/la053021l.

[29] Siddhartha K, Mukesh K, Amey W, Dasarathi D, Vimal KJ. Cyclopalladation of telluro ether ligands: synthesis, reactivity and structural characterization. Dalton Trans. 2014;43:16056. https://doi.org/10.1039/C4DT02200A.

[30] Arora A, Oswal P, Rao GK, Kumar S, Singh AK, Kumar A. Catalytically active nanosized PdTe (telluropalladinite) and PdTe (kotulskite) alloys: first precursor-architecture controlled synthesis using palladium complexes of organotellurium compounds as single source precursors. RSC Adv. 2021;11(13):7214. https://doi.org/10.1039/d0ra08732g.

[31] Zou XW, Fan HQ, Tian YM, Zhang MG, Yan XY. Chemical bath deposition of Cu_2O quantum dots onto ZnO nanorod arrays for application in photovoltaic devices. RSC Adv. 2015;5(30):23401. https://doi.org/10.1039/c4ra13776k.

[32] Ozaslan D, Ozkendir OM, Gunes M, Ufuktepe Y, Gumus C. Study of the electronic properties of Cu_2O thin films by X-ray absorption spectroscopy. Optik. 2018;157:1325. https://doi.org/10.1016/j.ijleo.2017.12.119.

[33] Zhang QK, Shao T, Li Y, Bai DH, Xue ZY, He SJ, Zhang DX, Zhou XB. One-step fabrication of bimetallic PtPd mesoporous nanospheres for methano electrooxidation. J Electroanal Chem. 2022;911: 116192. https://doi.org/10.1016/j.jelechem.2022.116197.

[34] Tang JX, Chen QS, You LX, Liao HG, Sun SG, Zhou SG, Xu ZN, Chen YM, Guo GC. Screw-like PdPt nanowires as highly efficient electrocatalysts for methanol and ethylene glycol oxidation. J Mater Chem A. 2018;6(5):2327. https://doi.org/10.1039/c7ta09595c.

[35] Li JX, Chang YJ, Li DZ, Feng LG, Zhang BG. Efficient synergism of V_2O_5 and Pd for alkaline methanol electrooxidation. Chem Commun. 2021;57(57):7035. https://doi.org/10.1039/d1cc02934g.

[36] Chen L, Lu LL, Zhu HL, Chen YG, Huang Y, Li YD, Wang LY. Improved ethanol electrooxidation performance by shortening Pd-Ni active site distance in Pd-Ni-P nanocatalysts. Nat Commun. 2017;8:9. https://doi.org/10.1038/ncomms14136.

[37] Li CL, Jiang B, Miyamoto N, Kim JH, Malgras V, Yamauchi Y. Surfactant-directed synthesis of mesoporous Pd films with perpendicular mesochannels as efficient electrocatalysts. J Am Chem Soc. 2015;137(36):11558. https://doi.org/10.1021/jacs.5b06278.

[38] Li HH, Zhao S, Gong M, Cui CH, He D, Liang HW, Wu L, Yu SH. Ultrathin PtPdTe nanowires as superior catalysts for methanol electrooxidation. Angew Chem-Int Edit. 2013;52(29):7472. https://doi.org/10.1002/anie.201302090.

[39] Ma SY, Li HH, Hu BC, Cheng X, Fu QQ, Yug SH. Synthesis of low Pt-based quaternary PtPdRuTe nanotubes with optimized incorporation of Pd for enhanced electrocatalytic activity. J Am Chem Soc. 2017;139(16):5890. https://doi.org/10.1021/jacs.7b01482.

[40] Ali A, Shen PK. Recent advances in graphene-based platinum and palladium electrocatalysts for the methanol oxidation reaction. J Mater Chem A. 2019;7(39):22189. https://doi.org/10.1039/c9ta06088j.

[41] Sarac B, Karazehir T, Ivanov YP, Putz B, Greer AL, Sarac AS, Eckert J. Effective electrocatalytic methanol oxidation of Pd-based metallic glass nanofilms. Nanoscale. 2020;12(44):22586. https://doi.org/10.1039/d0nr06372j.

[42] Bao YF, Liu H, Liu Z, Wang FL, Feng LG. Pd/FeP catalyst engineering via thermal annealing for improved formic acid electrochemical oxidation. Appl Catal B-Environ. 2020;274:119106. https://doi.org/10.1016/j.apcatb.2020.119106.

[43] Chen X, Granda-Marulanda LP, Mccrum IT, Koper MTM. How palladium inhibits CO poisoning during electrocatalytic formic acid oxidation and carbon dioxide reduction. Nat Commun. 2022;13(1):38. https://doi.org/10.1038/s41467-021-27793-5.

Springer Nature or its licensor (e.g. a society or other partner) holds exclusive rights to this article under a publishing agreement with the author(s) or other rightsholder(s); author self-archiving of the accepted manuscript version of this article is solely governed by the terms of such publishing agreement and applicable law.